Bulletin of the Seismological Society of America, Vol. 99, No. 6, pp. 3374–3389, December 2009, doi: 10.1785/0120080301

Rupture Process and Aftershocks Relocation of the 8 June 2008 M_w 6.4 Earthquake in Northwest Peloponnese, Western Greece

by K. I. Konstantinou, N. S. Melis, S.-J. Lee, C. P. Evangelidis, and K. Boukouras

Abstract On 8 June 2008 at 12:25 (GMT) an M_w 6.4 strong earthquake occurred in the area of northwest Peloponnese, western Greece, causing the death of two people and extensive damage to the surrounding area. The main event and its aftershocks were recorded by one nationwide and three regional networks equipped with three-component broadband seismometers. Initial locations of the earthquake sequence comprising 438 aftershocks showed a linear northeast–southwest trend and that the mainshock was located at 22 km depth. After the relocation using catalog and differential travel times, most events form three distinct clusters at depths 15–25 km. Moment tensor solutions for the main event and its largest aftershocks exhibited a pure strike-slip mechanism with one nodal plane orientated northeast–southwest in accordance with the relocated seismicity. A parallel, nonnegative least-squares inversion technique utilizing multiple-time windows was used to derive the spatiotemporal slip distribution of the main event. The resulting slip distribution model revealed a large slip patch (maximum slip ~150 cm) between 10 and 20 km depth at the northeast part of the fault that also coincides with the area that suffered most of the damage. Another patch exhibiting smaller amounts of slip (20–50 cm) is located to the southwest direction at the same depth range, and smaller patches exist at 25–30 km depth. Most aftershocks are located in areas of low slip (< 25 cm) filling the regions of slip deficit. The 8 June earthquake occurred at an area where no previous seismological or other observations indicated the existence of a seismogenic fault at that depth and with this strike. This, and the fact that the event nucleated in the middle to lower crust, may be interpreted as the reactivation of a fault structure that was inherited from previous tectonic phases.

Online Material: Spatiotemporal evolution of the aftershock sequence of the 8 June 2008 mainshock, sensitivity tests to the mainshock slip inversion, color versions of figures, relocated aftershocks catalog, classification scheme for the moment tensor solutions, and moment tensor inversion description.

Introduction

The tectonic setting of western Greece is dominated by two geodynamic processes, namely the collision of the Apulian microplate with the Eurasian plate in the northwest and the subduction of the African slab underneath the Eurasian plate near Zakynthos Island (Baker *et al.*, 1997; Haslinger *et al.*, 1999; Clément *et al.*, 2000; Sachpazi *et al.*, 2000; Laigle *et al.*, 2002) (Fig. 1a). The collision is responsible for the deformation by east–west shortening of the External Hellenides and the formation of fold-and-thrust belts during the Neogene. The area of northwest Peloponnese in particular comprises formations of the Gavrovo and Ionian isopic zones that are also part of the External Hellenides. Their stratigraphy indicates that they consist mainly of carbonate rocks, evaporites, and flysch. Skolis mountain (Fig. 1b) represents their tectonic boundary (Kamberis, Ioakim, *et al.*, 2000; Kamberis, Sotiropoulos, *et al.*, 2000, and references therein). Postcompressional normal faulting has affected the area since the Pliocene and resulted in the formation of a number of sedimentary basins to the west of Skolis mountain.

The seismicity of northwest Peloponnese can be considered low if compared to that of the nearby Ionian Islands of Kefalonia and Lefkada that are bordered to the west by the very active Kefalonia Transform fault (KFT). Catalogs of historical seismicity mention only one large event that occurred on 23 January 1806 causing considerable damage to the city of Patras (maximum intensity VIII), and the shock was felt in

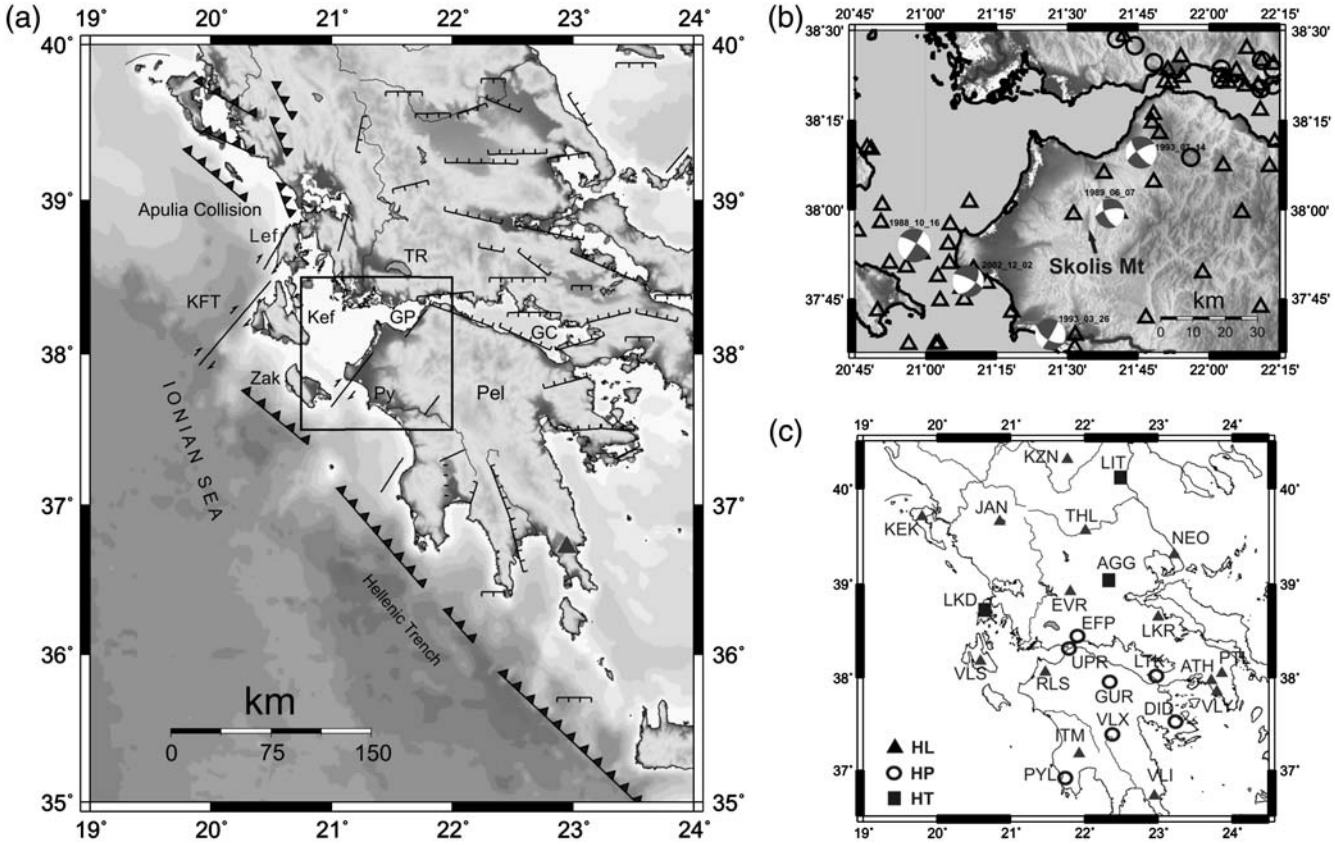

Figure 1. (a) Map showing the tectonic setting in western Greece. Major faults and plate boundaries have been adopted from Papazachos and Papazachou (1997). KFT, Kefalonia Transformation fault; Kef, Kefalonia Island; Lef, Lefkada Island; Zak, Zakynthos Island; GP, Gulf of Patras; Py, city of Pyrgos; Pel, Peloponnese. (b) Expanded view of the area inside the square shown in (a). Triangles indicate well-constrained locations, taken from Engdahl *et al.* (1998) (1964–2005), of events deeper than 10 km, and open circles indicate events shallower than that. The symbols represent focal mechanisms retrieved from the Global Centroid Moment Tensor (CMT) database (Table 1; see also the Data and Resources section) of earthquakes that have occurred in the area previously. (c) Map showing the locations of the stations used in this study. The different symbols correspond to different seismic networks. HL, network operated by the National Observatory of Athens–Institute of Geodynamics; HP, network operated by the University of Patras; HT, network operated by the University of Thessaloniki.

the broader area of northwest Peloponnese (Papazachos and Papazachou, 1997). During the instrumental era and for the period 1964–2005 the global relocation database of Engdahl *et al.* (1998) and its subsequent updates show that the seismicity is characterized by events with hypocentral depths that in most cases exceed 10 km (Fig. 1b) in agreement with the results of an earlier microseismic survey (Hatzfeld *et al.*, 1990). The small number of moderate size earthquakes ($M_w < 6$) means that only a handful of teleseismic moment tensor solutions are available and these are given in Table 1 and also shown in Figure 1b. Strike-slip motion seems to prevail on all these focal mechanisms confirming geodetic studies that show a significant clockwise rotation of the area (Le Pichon *et al.*, 1995; Cocard *et al.*, 1999; Hollenstein *et al.*, 2008).

On 8 June 2008 at 12:25 (hereafter all times are given in GMT), a strong earthquake occurred at northwest Peloponnese, and the shock was felt in most parts of Greece. The event caused two deaths and a hundred injuries, and 10,000 houses suffered small to severe damage, rail lines were benched, and liquefaction was observed at many sites (Kalogeras *et al.*, 2008; Margaris *et al.*, 2008). In this work we perform a detailed analysis of all available regional waveform data in order to elucidate the geometric fault properties and rupture process of this latest event. First, we describe the dataset used and report the initial results in terms of earthquake location and temporal distribution of seismicity. Later these results are refined through the use of a waveform cross-correlation (CC) relocation that allows a better delineation of the seismogenic fault. Point-source approximations for the mainshock and the largest aftershocks are derived by inverting the regional waveforms for the best-fitting moment tensor. A finite fault inversion of the waveform data is also performed yielding a slip distribution model for the mainshock. Finally, we close with a discussion of the rupture process of the main event and a seismotectonic interpretation for its occurrence.

Data and Initial Locations

Since 2007 a project has been initiated with the aim to link the main seismic networks that monitor seismicity in Greece into one Hellenic Unified Seismic Network (HUSN). Thus, HUSN will consist of a nationwide network operated by

Table 1

Summary of the Source Parameters of the Largest Events that Have Occurred in Northwest Peloponnese during the Past 30 yr (See Also Fig. 1b)

Date (mm/dd/yyyy)	Time	Longitude	Latitude	H (km)	M_w	ϕ_1	ξ_1	λ_1	ϕ_2	ξ_2	λ_2
10/16/1998	12:34:06	37.877	20.986	16	5.9	301	76	−3	32	87	−166
06/07/1989	19:45:55	37.991	21.682	23	5.2	154	64	−26	256	67	−152
03/26/1993	11:58:16	37.613	21.526	15	5.4	122	60	5	30	86	150
07/14/1993	12:31:50	38.212	21.826	18	5.6	238	73	−163	143	73	−18
12/02/2002	04:58:59	37.804	21.142	30	5.7	37	53	−163	297	76	−38

Origin times and locations have been obtained from Engdahl *et al.* (1998) and subsequent updates, and moment magnitude and focal mechanism information was taken from the Global CMT database (see the Data and Resources section). H represents the hypocentral depth; ϕ, ξ, λ are strike, dip, and rake, respectively, and the number indicates nodal plane 1 or 2.

the National Observatory of Athens, Institute of Geodynamics, and three regional seismic networks operated by the Universities of Athens, Thessaloniki, and Patras, respectively. The merged networks have seismic stations equipped with three-component seismometers. Absolute timing is provided by Global Positioning System (GPS) receivers. A mixture of sensor types is used including Lennartz Le-3D (20 sec), Guralp 40T (30/60 sec) /3ESP (60 sec) /3T (120 sec), Trillium (40/120 sec), and STS-2 instruments. All recorded signals are transferred via dedicated telephone or satellite connection lines in near real time to a collection center where they are stored for analysis. All four centers are linked in terms of exchanging their data in near real time, making data available to all partner centers. Figure 1c shows the institute operator for each station that was available and used in this study. At the time of the 8 June earthquake many stations were available; however, due to the strong ground motion, stations RLS and VLS and all the stations of the HP network were saturated in all three components.

We started the processing of the waveform data by manually picking the *P* and *S* phases of the recorded mainshock and its aftershocks for the period starting 8 June until 13 July, comprising of 438 events. All stations shown in Figure 1c were utilized in the phase picking procedure, and *P*- and *S*-phase picks from stations RLS and UPR (closest stations to the epicentral area) were included whenever possible. For the purpose of avoiding any systematic location bias due to the assumed velocity structure, we tested three different 1D models proposed for the area of western Greece. These models were derived by the tomographic studies of Melis and Tselentis (1998), Haslinger *et al.* (1999), and the surface wave dispersion study of Novotny *et al.* (2001). The picked arrival times were then inverted using HYPO2000 (Klein, 2002), utilizing each time one of the aforementioned velocity models. Figure 2 shows the results of these location trials in map view, along with the corresponding histograms of the distribution of root mean square (rms) residuals and horizontal/vertical errors. The average hypocentral shift in event locations after using these different models did not exceed 2.7 km. The comparison of these results reveals that the 1D velocity model of Melis and Tselentis (1998), as well as Novotny *et al.* (2001), exhibits smaller mean location errors and rms residuals than the model of Haslinger *et al.* (1999). Furthermore the locations stemming from the Melis and Tselentis model seem to have smaller mean vertical errors (~1.7 km) than the other two; therefore, we decided to use them as initial locations for the relocation process described in the next section.

Earthquake Relocation

In order to obtain more precise locations of this earthquake sequence, we used the *COMPLOC* package (Lin and Shearer, 2006) that applies a shrinking grid-search relocation algorithm using the source specific station term method (Richards-Dinger and Shearer, 2000; Lin and Shearer, 2005). The method accepts as input the initial location of events and their corresponding travel times, calculates iteratively station corrections for each source–receiver pair, and inverts for a new set of locations. These source specific station corrections are the weighted median of residuals at a given station from N nearby events. The number N and the maximum allowed distance between them is defined and reduced in subsequent iterations. In our case, it starts with 100 nearby events and a maximum cutoff value of 50 km and is reduced after 35 iterations to 10 nearby events and a maximum cutoff distance of 5 km. Differential travel times from waveform cross correlation (WCC) can also be included in the procedure allowing further constraints to be put in the inversion. These differential travel times are included as additional information to the observed arrival times in order to solve for a new set of adjusted picks by minimizing the misfit of both the original picks and the differential times (Shearer, 1997). This procedure requires a similar-event cluster identification and is termed by Shearer *et al.* (2005) as cluster analysis.

For the application of the WCC relocation method to the 8 June earthquake sequence, we include both catalog and differential travel times, and the Melis and Tselentis velocity model is used. Differential travel times are obtained after low-pass filtering of the waveforms at 5 Hz and using a time window of 3 sec around the *P* phase and 4 sec around the *S* phase. We cross-correlate waveforms of event pairs at each station recorded within an epicentral distance of 250 km. This value insures for the mainshock that nonclipped stations at longer distances are incorporated in the estimation of

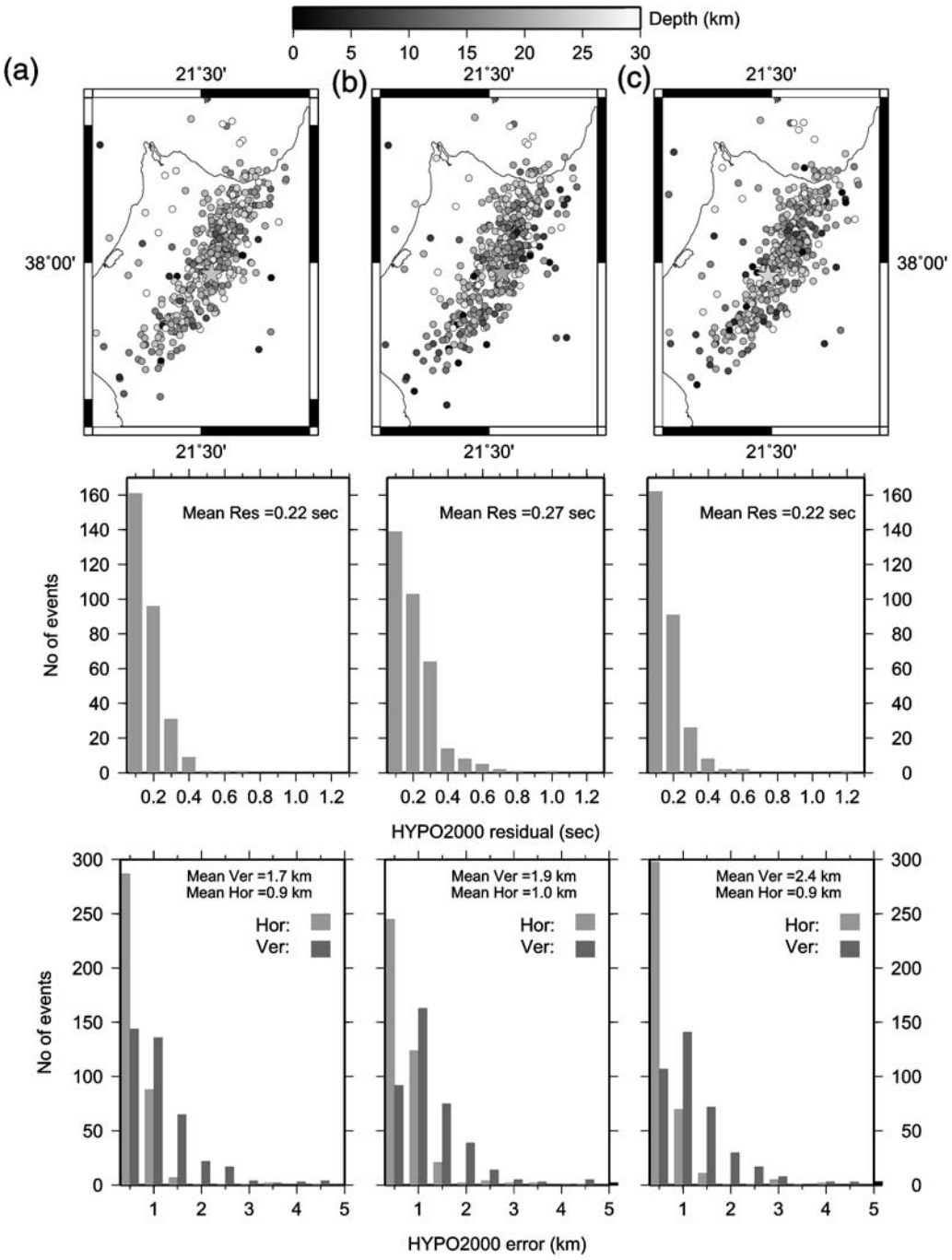

Figure 2. Maps of initial locations obtained from HYPO2000 along with corresponding distributions of rms residuals and vertical/horizontal errors using the velocity model of (a) Melis and Tselentis (1998), (b) Haslinger *et al.* (1999), and (c) Novotny *et al.* (2001). The depth of each event follows the gray scale shown at the top of the plot.

differential travel times and also that the mainshock is relocated in a similar way as its aftershocks. For each pair of events, waveforms from common stations are cross correlated and the value that is the average of the *P* and *S* CC coefficient is considered the CC value for this pair. An event pair is defined when there are at least three differential measurements for two events, and closely spaced events with average CC values higher than 0.6 in at least three stations define an event cluster. The choice of these values is a compromise between the highest relocation precision and the largest possible number of events that can be assigned to every cluster (Shearer *et al.*, 2003). The choice of a CC coefficient value of 0.6 results in 411 events that are finally relocated and assigned into 11 clusters. Individual CC coefficients appear to be higher for the *P* rather than the *S* phases (Fig. 3a), which probably implies a contamination of the *S* onset from the *P* coda. On the other hand, the distribution of the number of stations with average CC coefficients higher than 0.55 exhibits a peak

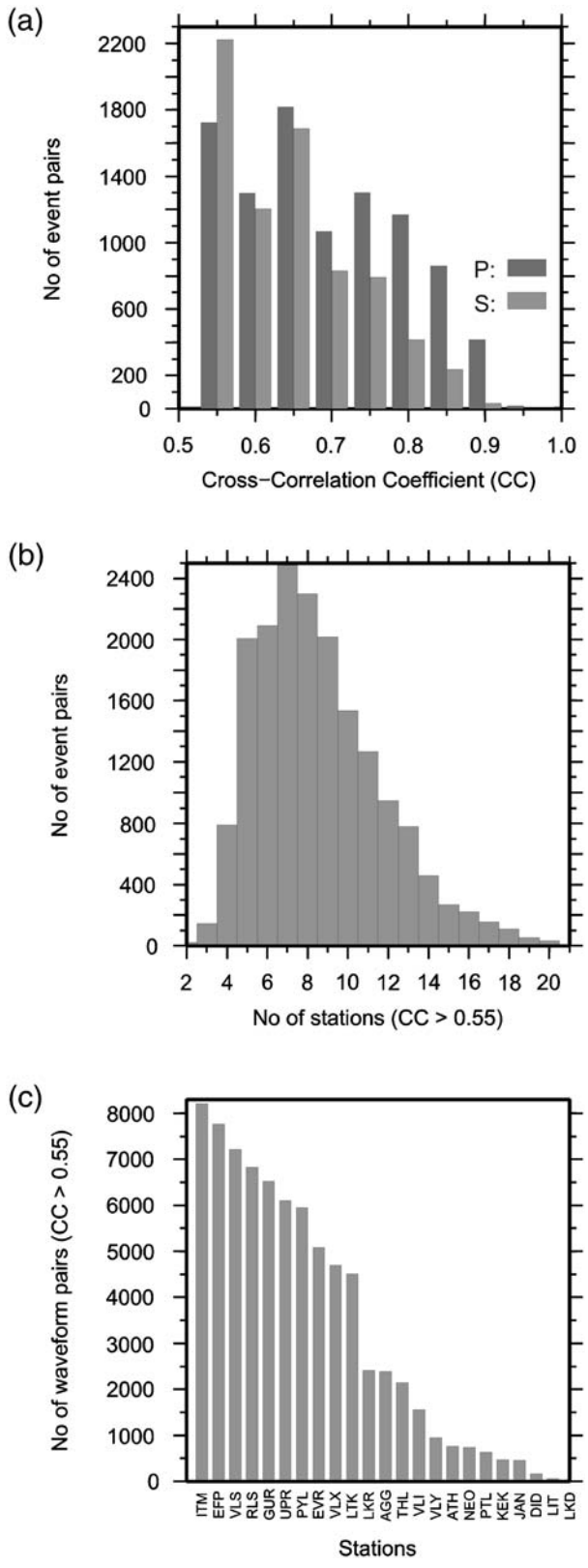

Figure 3. Histograms showing (a) the distribution of CC coefficients for *P* and *S* phases; (b) the distribution of the number of stations that had an average CC coefficient (for *P* and *S* phases) higher than 0.55; and (c) the distribution of the number of waveform pairs with average CC coefficients higher than 0.55 at the different stations used in this study.

around 7, and this happens mostly at stations ITM, EFP, RLS, GUR, UPR, and PYL (Fig. 3b,c).

Figure 4 shows a map and corresponding depth cross sections of the relocated mainshock–aftershocks sequence. It can be seen that most of the seismicity is expressed in the form of three distinct clusters and that the mainshock is relocated to the southwest at a hypocentral depth of 18 km. Most of the aftershocks have hypocentral depths comparable to the mainshock and in the range between 15 and 25 km. We estimate uncertainties for these relative locations using a bootstrap technique where random errors (drawn from a normal distribution) are added to the picks and each event is relocated 200 times (see Shearer, 1997; Evangelidis *et al.*, 2008). This procedure will result in a cloud of locations for whose horizontal and vertical scatter can be used in order to estimate errors. The mean values for the horizontal and vertical bootstrap error in our dataset are found to be 0.8 km and 1.1 km, respectively (Fig. 5). In order to investigate the spatial distribution of the aftershocks sequence as a function of time we also plotted depth cross sections for different time periods starting on 8 June ending on 13 July (Ⓔ Fig. S1, available in the electronic edition of *BSSA*). The results show that seismic activity started in all three clusters almost simultaneously after the mainshock and that the clusters remained active until the end of our study period. Ⓔ Table S1, available in the electronic edition of *BSSA*, contains the catalog of relocated events along with their bootstrap error estimates. Local magnitudes for all relocated events are also included in the supplement, calculated with their new hypocentral locations using simulated Wood–Anderson traces and following Melis and Konstantinou (2006) for magnitude calculation.

At this point it is necessary to examine more carefully the initial and relative locations of the main event that are summarized in Table 2. The epicentral shift between the initial location estimates using different velocity models is in the range of 0.7–4.2 km, and the hypocentral shift is 3–4 km. Such small differences probably indicate that the influence of the assumed velocity model on the absolute location of the main event is not so important. On the other hand, the WCC relocation yields a location to the southwest of the initial locations and at a hypocentral depth of 18 km. While this hypocenter is inside the vertical error bounds of the initial locations (the shallowest location depth is 19 km ± 1 km of error), the relocated epicenter is shifted several kilometers to the southwest. Theoretically, we expect that the relocation would produce a much more precise location for the main event because it incorporates additional independent information (catalog and WCC travel times) that was not utilized during the initial location. Nevertheless, we will further investigate the accuracy of this location later in this study by checking its influence on the finite fault inversion results.

Moment Tensor Inversion

A linear, time-domain moment tensor inversion method with a point-source approximation is applied to model the

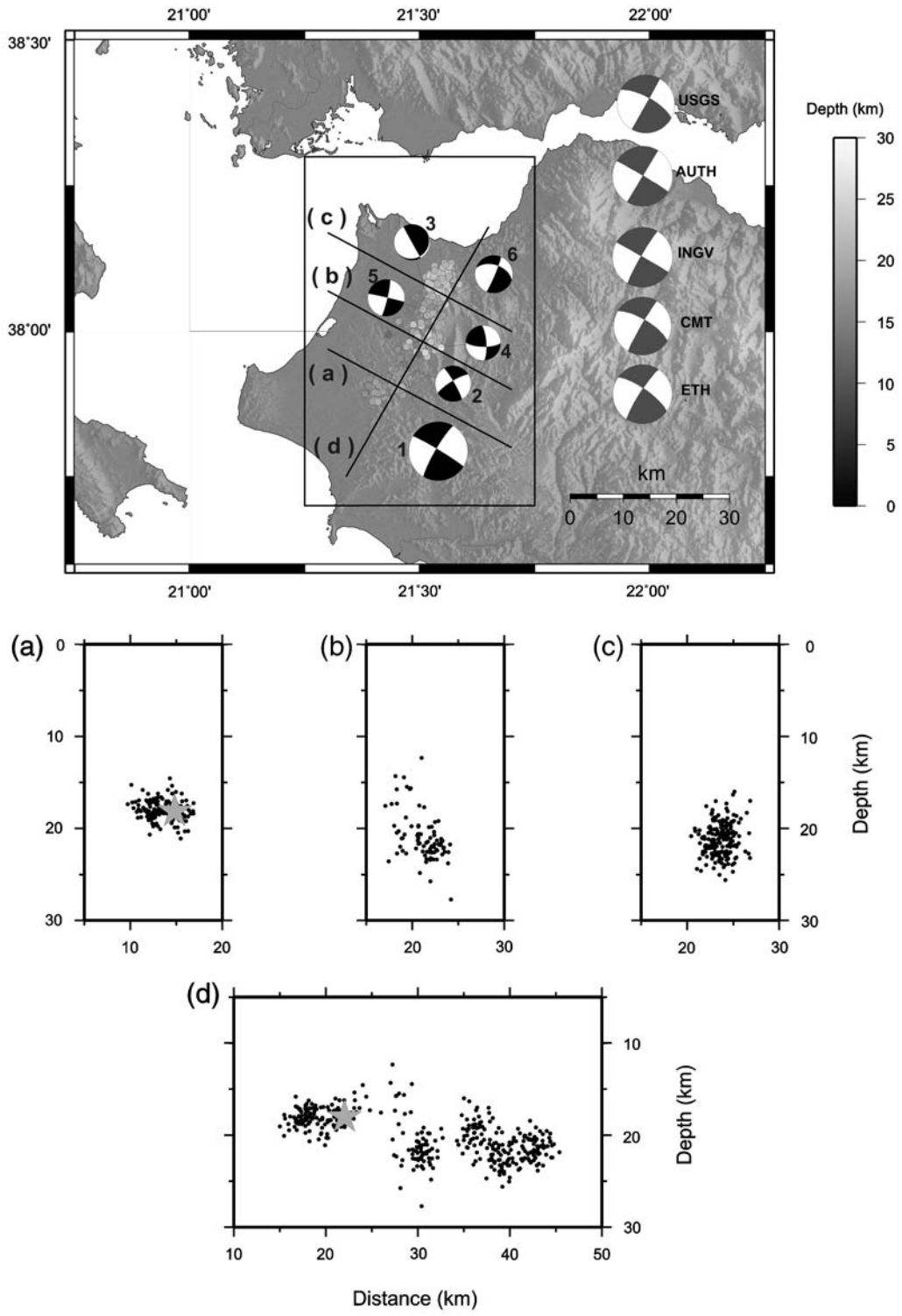

Figure 4. Map showing the results of the WCC relocation for the mainshock (star) and 411 aftershocks (filled circles). The depth of each event follows the gray scale shown at the right of the plot. Depth cross sections indicated by letters on the map are shown at the bottom. The symbols shown are the focal mechanism solutions for the main event and five aftershocks obtained in this study after waveform inversion (see text for more details). Each symbol is scaled according to the moment magnitude of the event, and the number corresponds to the numbering in Ⓔ Table S3 (available in the electronic edition of *BSSA*). Also shown at the right-hand side of the map are the focal mechanism solutions for the mainshock reported by different agencies (see also Table 3).

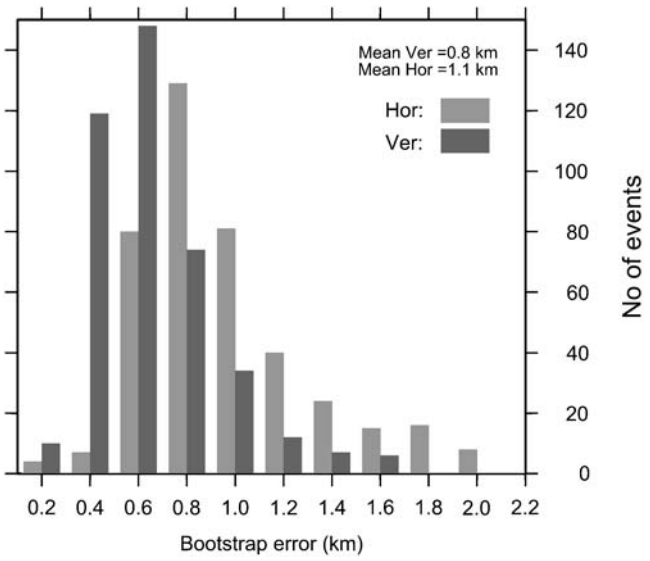

Figure 5. Histogram showing the distribution of the bootstrap error for the relocated events in both the horizontal and vertical direction (see text for more details).

three-component waveforms of the main event and of its five largest aftershocks (Randall *et al.*, 1995; Ghose *et al.*, 1998; Stich *et al.*, 2003). We calculated Green's functions using the reflectivity method of Kennett (1983) as implemented by Randall (1994) utilizing the velocity model of Haslinger *et al.* (1999) for paths that traverse western Greece and that of Novotny *et al.* (2001) for paths traversing the Peloponnese/central Greece. Data preparation prior to inversion includes the reduction of velocity waveforms to displacement and rotation of horizontal components into radial and transverse. The rotation is performed with respect to the epicenter stemming from the relocation procedure described in the previous section. Both the observed waveforms and the Green's functions are band-pass filtered between 0.05 and 0.08 Hz using a two-pole Butterworth filter and aligned according to their arrival times in order to minimize the effects of the assumed velocity structure and any source mislocation. The choice of this particular frequency band for performing our inversions is a compromise between the available bandwidth of some of our instruments (e.g., Lennartz Le-3D sensors broadband up to 20 sec) and the necessity to include longer periods in the inversion because modeling of waveforms at higher frequencies is very sensitive to the assumed velocity model.

The waveforms are inverted for the best-fitting deviatoric moment tensor assuming a delta source time function. This assumption breaks down for the main event of the sequence; therefore, we convolved its Green's functions with a trapezoid of appropriate length prior to the inversion. At first, inversions were performed at a coarse depth interval of 5 km followed by a finer one every 1–2 km around the depth that exhibited the minimum misfit. The criteria for including a station in the inversion were (1) its azimuth relative to the epicenter so that different parts of the focal sphere could be covered and (2) its epicentral distance, which should not exceed 250 km so that the source–receiver structure could be successfully approximated by our simple 1D velocity models. We evaluate the quality of the moment tensor solutions by jointly considering their average misfit (quality range A–D, with A indicating a misfit lower than 0.3 and D indicating larger than 0.7) and compensated linear vector dipole (CLVD) amount that is a measure of the non-double-couple part of the solution (quality range 1–4, with 1 indicating a CLVD percentage smaller than 20% and 4 indicating larger than 80%). The complete information for this quality scheme is given in Ⓔ Table S2, available in the electronic edition of *BSSA*. As an additional quality constraint we also consider the stability of the focal mechanism at the depths surrounding the minimum misfit depth.

Six stations (ATH, JAN, KEK, KZN, THL, and VLI) covering an azimuth of almost 180° around the epicenter were used for deriving the moment tensor solution of the mainshock. The misfit-versus-depth curve shows a relatively flat area in the range 15–27 km with a weak minimum at 24 km, while the misfit-versus-CLVD curve has a sharp minimum at 22 km (Fig. 6). Previous studies indicate that in the case when a solution depth cannot be determined solely by the misfit difference, then the CLVD percentage can be used as a constraint (e.g., Ghose *et al.*, 1998). Our preferred solution is therefore the one at 22 km depth showing an almost pure strike-slip mechanism. The quality of this solution falls

Table 2

Summary of Initial Location Results for the Mainshock of 8 June 2008 Using Three Different Velocity Models in each Hypo2000 Run and the Relative Location Obtained by WCC

Model	Longitude	Latitude	Depth (km)	ErrH (km)	ErrV (km)	rms (sec)
Initial Location Estimates						
Melis and Tselentis (1998)	21.523	37.978	22	0.5	1	0.3
Haslinger *et al.* (1999)	21.530	37.980	19	0.7	1	0.4
Novotny *et al.* (2001)	21.492	37.975	24	0.6	0.9	0.2
Relative Location						
Melis and Tselentis (1998)	21.46	37.924	18	1.02	0.79	

ErrH and ErrV are the resulting horizontal and vertical errors, respectively, given by HYPO2000, and the errors shown for the relative location correspond to the bootstrap error estimates (see text for more details).

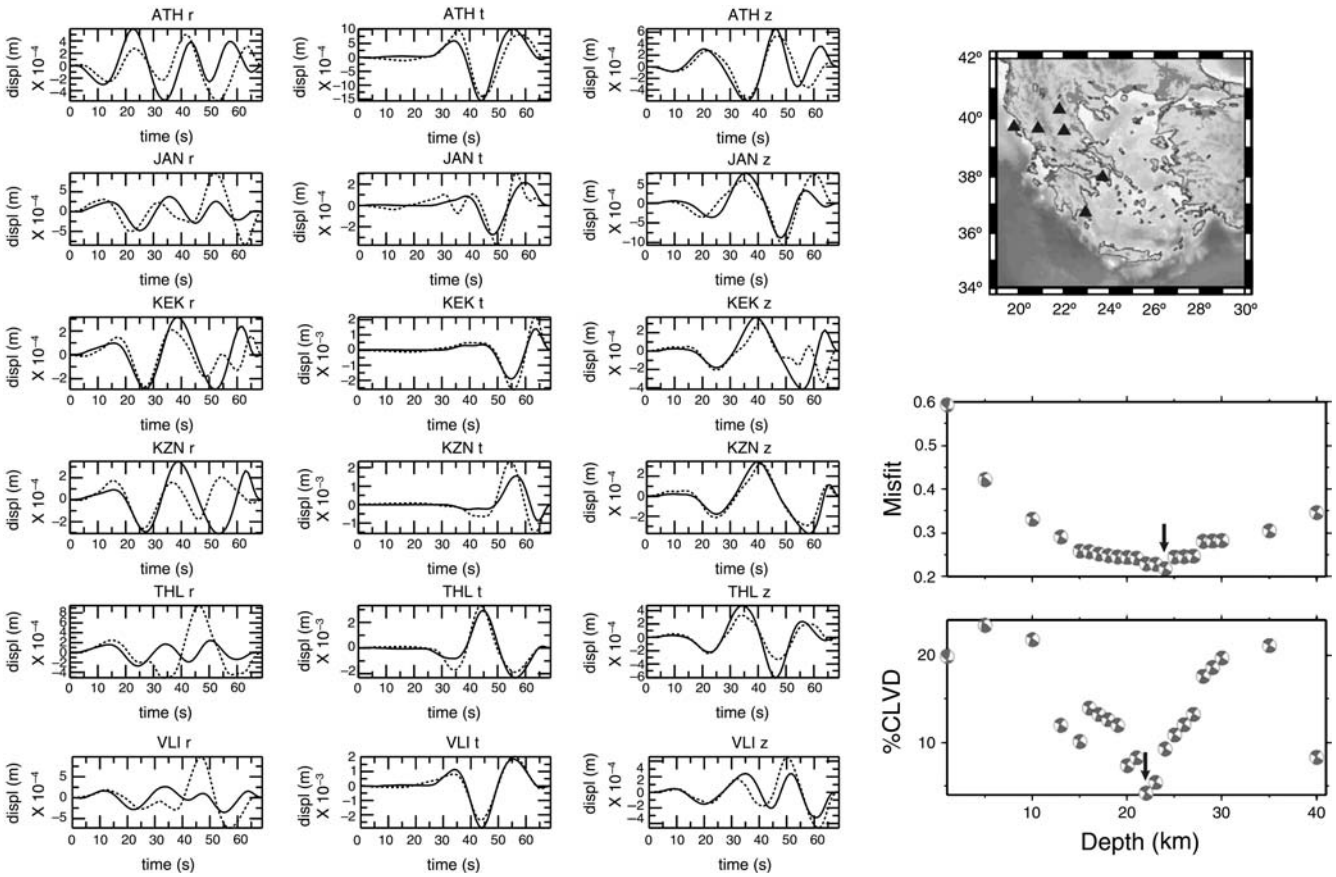

Figure 6. Moment tensor inversion results for the 8 June main event. On the left-hand side of the figure are the observed (solid curves) versus synthetic (dotted curves) seismograms obtained after the inversion for each station for a depth of 22 km. The map shows the location of the event (star) and the location of the stations used in the inversion (black triangles). The two diagrams represent the misfit-versus-depth and CLVD-versus-depth variations of the resulting solutions. The preferred focal mechanism solution is highlighted by a black arrow.

within the A1 category (misfit 0.23, CLVD 4.2%), while the focal mechanism is particularly stable for a range of depths. Several agencies (Global Centroid Moment Tensor [CMT], U.S. Geological Survey [USGS], Italian National Institution of Geophysics and Vulcanology [INGV], Swiss Seismological Service [ETH], and Aristotle University of Thessaloniki [AUTH]) have reported moment tensor solutions for the 8 June main event, and these are shown in Figure 4 and summarized in Table 3. By using the Kagan angle (Kagan, 1991) to quantify the degree of similarity between two focal mechanisms, we find that our preferred solution differs from them only by few degrees (4°–16°). It should be noted that the CLVD component reported in these solutions is on the order of 0%–13% with the exception of ETH, which reports a larger amount (~34%). The small CLVD amount reported by most agencies is confirmed by our moment tensor results and supports the view that the source of the 8 June event did not exhibit any significant geometric complexity or anomalous nature. The distribution of relocated aftershocks provides clear evidence that the nodal plane striking northeast–southwest is indeed the ruptured fault plane (see also Fig. 4).

The waveforms of the five aftershocks were inverted in the same way as these of the main event using 4–5 stations in each case (mostly ATH, JAN, LIT, and THL). The qualities for most solutions are A1, A2, or B1, and only one event exhibits a C1 quality. The resulting solutions show in most cases strike-slip mechanisms and minimum misfit depths at 15–21 km, similar to the results derived for the mainshock (Fig. 4). A detailed table containing all information concerning the moment tensor inversion results (including misfit/CLVD-versus-depth curves and seismogram fits) for all events can be found in the Ⓔ electronic edition of *BSSA* (Table S3).

Finite Fault Inversion

Finite fault inversion problems are usually formulated in the well-known linearized form, $\mathbf{Ax} = \mathbf{b}$ where $\mathbf{A}$ is the matrix of the Green's functions, $\mathbf{b}$ is the observed data vector, and $\mathbf{x}$ is the vector of slip on each subfault that satisfies the problem (e.g., Hartzell and Heaton, 1983) (Fig. 7). An important improvement to this approach is the introduction of multiple-time windows into the inversion problem, resulting in a better spatiotemporal resolution of slip. This is accomplished first by forming the columns of matrix $\mathbf{A}$ as the Green's functions strung end to end for each subfault and

Table 3
Summary of Source Parameters and Focal Mechanism Solutions Reported by Different Agencies for the 8 June 2008 Earthquake

Agency*	Latitude	Longitude	Depth (km)	M_w	M_0 (dyn-cm)	Strike	Dip	Rake	% CLVD
ETH	38.01	21.44	31	6.4	5.17E+025	305	75	8	34
CMT†	37.97	21.60	15	6.3	3.89E+025	301	72	4	2
INGV†	37.99	21.52	38	6.5	6.00E+025	300	89	5	13
AUTH	37.97	21.50	30	6.5	6.51E+025	301	88	0	0
USGS	38.14	21.59	10	6.3	3.10E+025	299	71	0	12

*ETH, Swiss Seismological Service; CMT, Global Centroid Moment Tensor; INGV, Italian National Institute of Geophysics and Volcanology; AUTH, Aristotle University of Thessaloniki; USGS, U.S. Geological Survey.
†Centroid location and depth is reported.

for all the stations in the inversion. In a similar way matrix **b** is formed by stringing all observation records end to end. Subsequently, matrix **A** is rearranged by taking Nt time windows and putting them side by side, while vector **x** becomes Nt times the single-time window, where Nt is the number of windows (Fig. 7). An increase in the number of time windows would lead to a large expansion of matrix **A** making the solution of this problem very costly in terms of computer time. Program performance can be improved by applying a parallel nonnegative least-squares (NNLS) inversion technique that decomposes matrix **A** into different computing nodes and solves for vector **x** for each time window. All slip on the fault must be initiated after the rupture front has passed through, so that the source duration time starts counting after this rupture delay time. In this multiple-time window analysis, each subfault is allowed to slip in any of the 2 sec time windows following the passage of the rupture front while each window may have an overlap of 1 sec. Further information about this method and its application to finite fault inversion problems can be found in Lee *et al.* (2006) and Konstantinou *et al.* (2009).

We applied the method described previously to our main event after carefully selecting suitable waveform data to include in the inversion. The criteria for suitability take into account the azimuthal coverage, the epicentral distance (so that the source–receiver structure could be approximated by 1D velocity models), and possible amplitude saturation effects of the recorded waveforms. In this way we were able to include in the inversion nine stations (KZN, KEK, JAN, THL, NEO, LKR, ATH, ITM, and VLI) and the north–south component of station EVR (see Fig. 1c). This station distribution provides the best-possible azimuthal coverage leaving a gap only toward the southwest direction of the Ionian Sea. The instrument response was removed from the recorded signals, the waveforms were filtered between 0.05 and 0.125 Hz using a four-pole Butterworth filter and decimated to 1 sample per second. Green's functions were calculated by the frequency–wavenumber method, utilizing the same velocity models that were used for the moment tensor inversion. Once the Green's functions were computed they were filtered between 0.05 and 0.125 Hz in the same way as the observed data. The fault was parameterized by subfaults, each having a dimension of 3×3 km^2 covering an area of length and down-dip width of 66 and 42 km, respectively. These values of length and down-dip width were chosen for the purpose of avoiding any underestimation of the true fault plane. We also use the moment tensor solution determined in this study in order to account for the source radiation effects. The rupture velocity was initially set to 3 km/sec, but it was allowed to vary during the inversion. The number of time windows to be used was set to 24. Additionally, we imposed some stability constraints such as minimization of the seismic moment to the value derived in this study (0.449×10^{26} dyne cm) and damping at the edge of the parameterized fault in order to avoid unrealistic slip distributions.

Figure 8 shows the results (slip distribution and moment rate function) of the finite fault inversion for the 8 June main event using all the aforementioned parameters. We conducted several tests for the purpose of investigating the robustness and stability of this slip model when one of the inversion parameters was changed. First, we performed a resolution test where we tried to resolve *a priori* slip patches that vary in dimension, slip amplitude, and depth, using three different subfault dimensions (3×3, 4×4, and 5×5 km^2). The synthetic slip model consisted of three patches, the smallest of them having a dimension of 12×9 km^2 while the lowest slip amplitude considered was on the order of 20 cm (Fig. 9). Synthetic waveforms were computed for each of our stations using forward modeling, and these were subsequently inverted in the same way as in our preferred slip model (i.e., frequency band 0.05–0.125 Hz, 24 time windows, the moment tensor solution derived in this study, and location determined by the WCC method). We find that in the case of the 3×3 km^2 subfault dimension the synthetic patches are adequately resolved even though the smallest patch appears somewhat distorted and contains an area of larger slip. In the cases of 4×4 and 5×5 km^2, resolution deteriorates significantly, and it is not possible to recover either the correct shape or slip value of the synthetic patches.

We also tried to determine the optimum number of multiple-time windows that can be used in order to resolve the slip in both time and space. A set of inversions with multiple-time windows in the range of 1–36 were carried out, and the results are summarized in Ⓔ Figure S2,

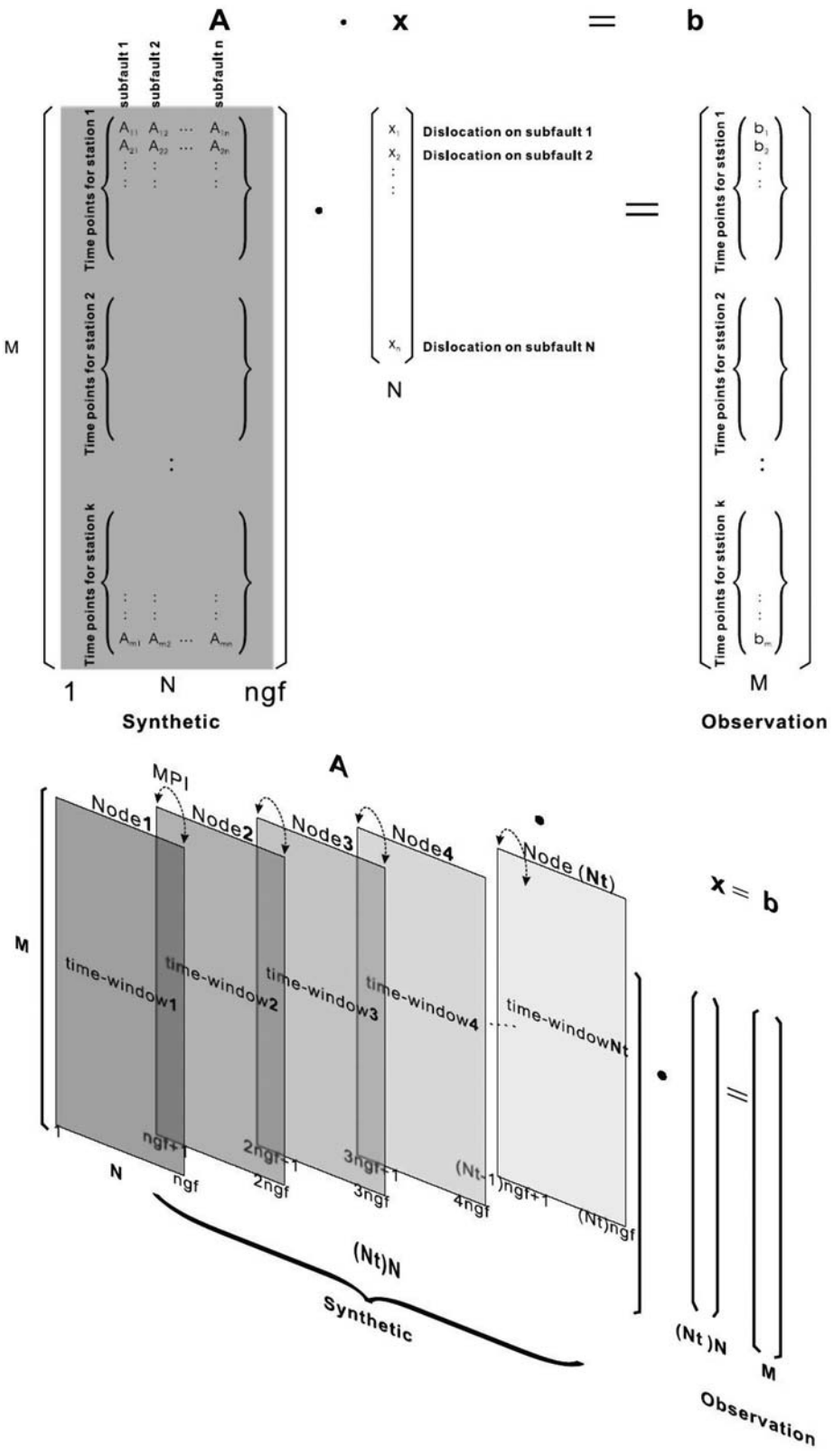

Figure 7. Upper panel: traditional single-time window matrix system used by previous studies to solve for the slip distribution along a fault (see text for details). Lower panel: multiple-time window approach where matrix **A** is decomposed in the parallel NNLS inversion. Message passing interface is applied as the communicant between the computing nodes in the parallel computing process (from Lee *et al.*, 2006).

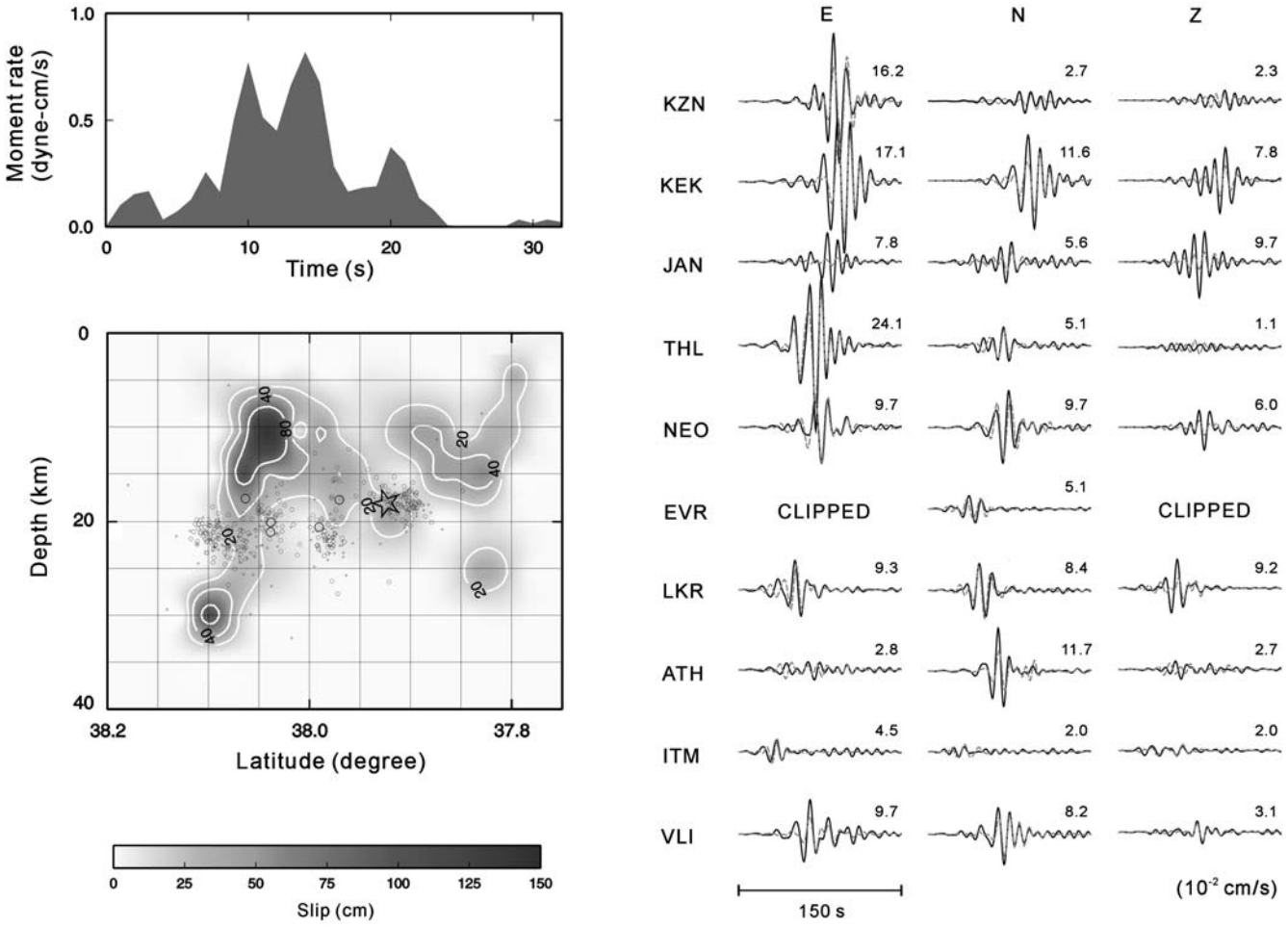

Figure 8. Summary of results stemming from the finite fault inversion of the 8 June main event. Slip values vary according to the gray scale shown at the bottom of the figure. The star indicates the relocated hypocenter of the mainshock, and the open circles indicate the relocated aftershocks. The moment rate function is shown at the left-hand corner of the plot. The fit of observed (black curves) versus synthetic (gray curves) waveforms can be seen at the right-hand side of the plot. The numbers above each trace represent the maximum amplitude multiplied by 10^{-2} cm/sec. Ⓔ A color version of this figure can be found in the electronic edition of *BSSA*.

available in the electronic edition of *BSSA*. It can be seen that at least 18 time windows are needed in order to minimize the misfit and sufficiently resolve both the temporal and spatial slip pattern. An increase of the number of time windows beyond this value apparently does not result in any significant improvement of the solution. The next test has to do with the stability of the slip model when a different combination of stations is used in the inversion. We performed another set of inversions excluding one station at a time and subsequently taking the average of the resulting slip distributions (Ⓔ Fig. S3, available in the electronic edition of *BSSA*). It is expected that this averaging will smooth any artifacts introduced by any particular station and sharpen the features that are common in all solutions. Ⓔ Figure S4, in the electronic edition of *BSSA*, compares this average slip model with the slip distribution obtained from the inversion of all available waveform data. It can be seen that both of them are quite similar, and there are only slight differences in the exact shape of the resolved slip patches.

Another point that we investigated regarding the robustness of the slip results is whether our finite fault inverse problem is underdetermined or not. In order to check this we decimated the observed waveform data every 0.5 sec instead of the initial decimation of 1 sample per second. In this way matrix **A** attains a dimension of $22,400 \times 16,560$ with its number of rows (number of equations) being larger than its number of columns (number of unknown dislocations on subfaults) (see Fig. 7). We invert the new matrix using the same parameters as before and compare the results with our preferred slip model (Ⓔ Fig. S5, available in the electronic edition of *BSSA*). It can be seen that the two models have very similar misfits (0.3736 and 0.3898, respectively) and look almost the same. Finally, a test is performed where we invert the data using as epicenter and focal depth the ones stemming from HYPO2000. The results show that the resulting slip distribution is less resolved and the overall misfit is much higher (~0.5037) when compared with the preferred model that uses the location parameters stemming from

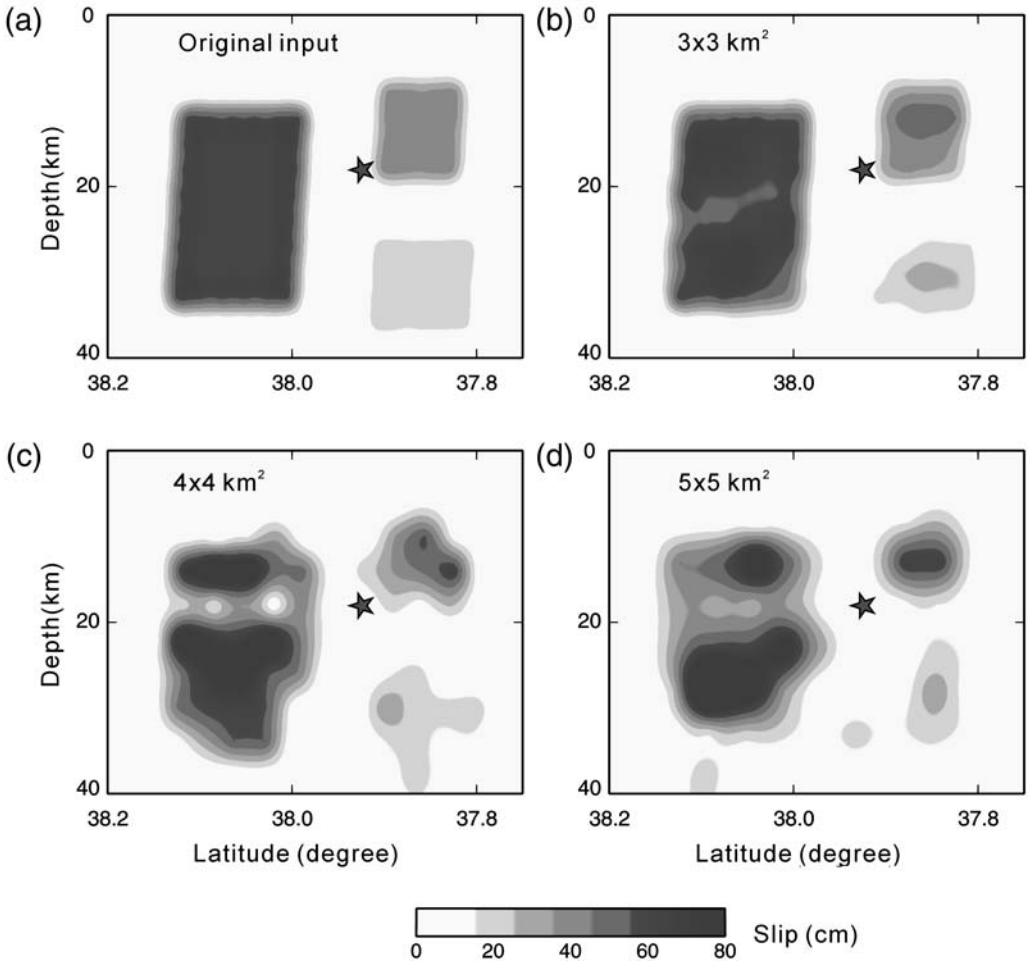

Figure 9. Results of the resolution test performed in this study: (a) synthetic patches model that was used for the forward modeling of waveforms at each station, (b) finite fault inversion results using a subfault size of 3×3 km^2, (c) the same for subfault size 4×4 km^2, and (d) the same for subfault size 5×5 km^2. The slip values vary according to the gray scale shown at the bottom of the plot. Ⓔ A color version of this figure can be found in the electronic edition of *BSSA*.

the WCC relocation (Ⓔ Fig. S6, available in the electronic edition of *BSSA*). This implies that the data is better fit by assuming the latter location as the initiating point of the rupture on the fault plane.

Slip Distribution and Rupture Process of the Mainshock

The resulting slip distribution pattern for the 8 June event consists of a number of patches of different sizes that are located at various depths (Fig. 8). The largest patch that also exhibits the highest values of slip (~150 cm) extends from about 7 to 20 km depth and is located south of the Gulf of Patras, in the area of Kato Achaia. The location of the largest patch in that area and its high maximum slip value is in agreement with two other independent observations. First, eyewitness accounts and field surveys after the earthquake indicate that Kato Achaia is the area that was shaken most violently and sustained much damage to its buildings (Margaris *et al.*, 2008). Second, Newman *et al.* (2008) used teleseismic data recorded at 68 stations in order to calculate the radiated seismic energy of the 8 June event and its corresponding energy magnitude (M_E) as described by Choy and Boatwright (1995). The authors found that M_E was in the range 6.6–6.9 implying that the event radiated far more energy than what is expected for an M_w 6.4 earthquake. They also suggested that this characteristic is due either to unusually high slip or increased crustal rigidity. The former explanation seems to corroborate our finding of a well-resolved patch of unusually high slip beneath Kato Achaia.

A second large patch of lower slip values (20–50 cm) appears further southwest, extending in the same depth range as the Kato Achaia patch but with an undulating upper edge. Between these two patches lies the mainshock hypocenter that seems to be on top of a smaller slip patch. Two smaller patches that are located at greater depths (25–30 km) can also be seen. Even though their size is smaller than the size we used in our resolution test, they probably represent real features because they appear in all other tests we have conducted previously. When plotted on top of the slip distribution, the relocated aftershocks generally coincide with the areas of low slip

(< 25 cm) between the resolved slip patches. A preliminary dislocation model reported by Briole *et al.* (2008) puts the upper edge of the ruptured fault at a depth of 10 km, which generally agrees with our preferred slip model where most of the slip is concentrated at depths larger than 7 km.

The rupture process of the main event can be visualized by creating a series of snapshots that show how the slip distribution evolved through time on the fault plane (Fig. 10). During the first 4 sec small patches of slip appear around and below the main event hypocenter, corresponding to the small initial peak that is seen in the moment rate function. At around 8 sec small patches are formed in the southwest direction of the fault and at 12 sec slip starts initiating at the northwestern part of the rupture. The large slip patch beneath Kato Achaia is finally formed at 16 sec, a time that coincides with the maximum moment release as shown in the moment rate function. The second patch to the southwest of the fault plane is formed almost at the same time (12–16 sec), even though it takes its final shape 4 sec later (~20 sec). After this time the slip distribution pattern changes very little and the amount of moment that is released also drops significantly.

Seismotectonic Interpretation

Western Greece is an area where geodetic studies have complemented seismological observations in order to produce a consistent kinematic model. The most recent velocity field derived from long-term GPS measurements is reported by Hollenstein *et al.* (2008) and is shown in Figure 11 along with other tectonic and seismological information. Based on similar magnitude and direction of velocities, a clockwise rotating block is defined that encompasses the Ionian Islands of Lefkada, Kefalonia, and a part of mainland Greece. This block is bounded to the west by the KFT, to the north by the Amvrakikos fault (AF), and to the east by the Katouna fault (KF) that is believed to be a sinistral strike-slip fault. Seismicity seems to confirm such an interpretation, because most earthquakes occur at the boundaries and only a few of them originate between the Ionian Islands and mainland Greece (see also Hatzfeld *et al.*, 1995). This kinematic pattern becomes less clear when the Gulf of Patras is taken into consideration because there is no GPS-derived velocity field information for this area and seismicity is low. The Gulf

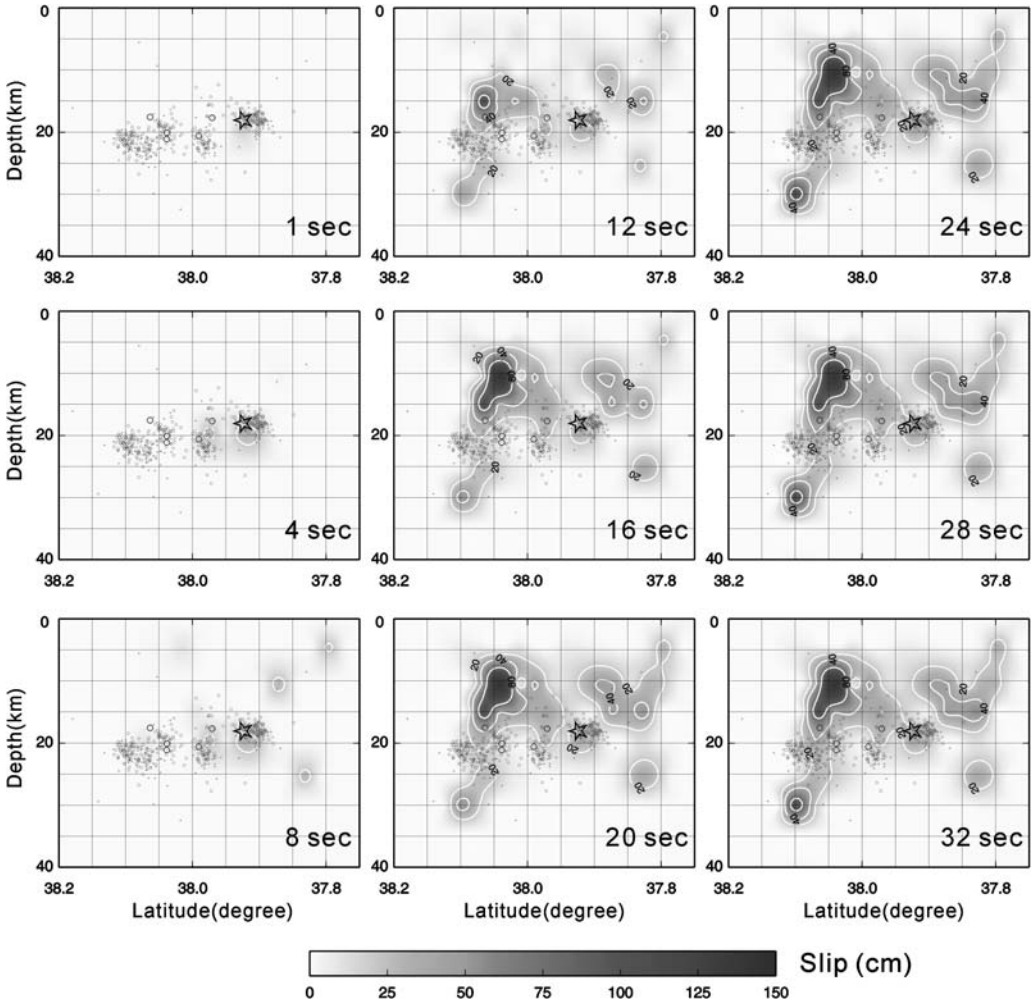

Figure 10. Snapshots of the rupture process of the 8 June earthquake depicted every 4 sec. Symbols plotted are the same as in Figure 8. Ⓔ A color version of this figure can be found in the electronic edition of *BSSA*.

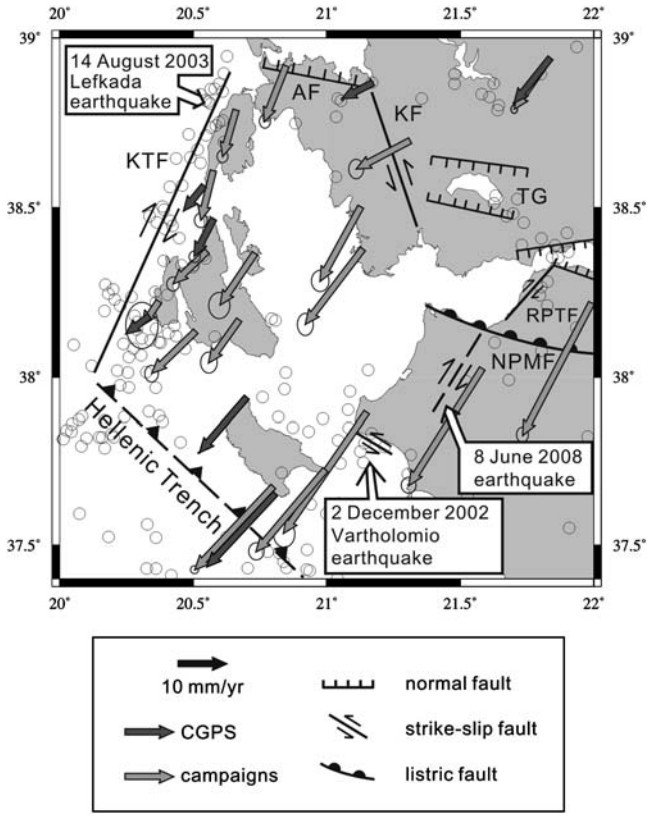

Figure 11. Synthesis of the available tectonic, seismological and geodetic information about western Greece. The tectonic elements shown on the map are adopted from numerous studies (Hatzfeld *et al.*, 1995; Papazachos and Papazachou, 1997; Haslinger *et al.*, 1999; Flotté *et al.*, 2005). The symbols for the different kind of faults are given in the legend. Open circles represent well-constrained earthquake epicenters obtained from the global relocation database of Engdahl *et al.* (1998) for the period 1964–2005. The 8 June 2008 earthquake fault and faults of other significant events in the area are highlighted. The GPS-derived velocity field published by Hollenstein *et al.* (2008) is also superimposed on the map. Each arrow indicates the direction and amount of velocity at a specific site, and the error ellipses represent the 1-sigma confidence region. The arrows are derived either from continuous GPS or campaign GPS data. Acronym key: KTF, Kefalonia Transform fault; AF, Amvrakikos fault; KF: Katouna fault; TG, Trichonis graben; RPTF, Rion-Patras Tranfer fault; NPMF, northern Peloponnese Major fault.

of Patras is bounded to the east by a northeast–southwest transfer zone (Rion-Patras Transfer fault [RPTF]) that accommodates the different rates of extension between the Corinth and Patras grabens and to the south by a major aseismic listric fault (Northern Peloponnese Major fault [NPMF]) that traverses northern Peloponnese (Melis *et al.*, 1989; Melis *et al.*, 1995; Sorel, 2000; Flotté *et al.*, 2005). Therefore, the Gulf of Patras may be considered as a smaller autonomous aseismic block within the Ionian Islands block.

Further to the south, northwest Peloponnese exhibits a velocity field similar in direction to that of the Ionian Islands block but having a larger magnitude (~30 mm/yr). The seismicity between northwest Peloponnese and the island of Kefalonia is also quite low, and no major fault can be identified in that area. This indicates that northwest Peloponnese may be also part of the Ionian Islands block, a suggestion made previously by Le Pichon *et al.* (1995) based solely on geodetic observations. The southern boundary of this block is probably defined by the seismicity increase at the strait between Zakynthos Island and the coast of Peloponnese where several moderate events occurred in the past (Figs. 1b and 11), including the 2 December 2002 (M_w 5.6) Vartholomio earthquake. Analysis of this earthquake by Roumelioti *et al.* (2004) showed that it was a sinistral strike-slip event with a fault plane striking northwest–southeast. This fault probably acts as the southern boundary of the Ionian block.

These observations imply that the block that comprises Lefkada, Kefalonia, part of mainland Greece, and northwest Peloponnese rotates clockwise as a whole and has a smaller velocity magnitude at its western part compared to the southeastern part. The 14 August 2003 (M_w 6.2) Lefkada earthquake changed this velocity deficit, introducing a maximum coseismic slip of 34 cm (Benetatos *et al.*, 2007) at the western part of the Ionian block. This is likely to have caused the accumulation of some deformation at the rigid inner part of the block that was probably diffused by distributed minor faulting, as suggested by analog models of rotating blocks (Goldsworthy *et al.*, 2002). However, the deformation at the borders of the block should have been greater, promoting the rupture of the fault zone that generated the 8 June event. The large nucleation depth of the June earthquake points to the possibility that this fault zone may be inherited from previous tectonic phases and reactivated as a strike-slip fault under the present-day clockwise rotation of northwest Peloponnese. Numerous studies have shown that the localization of deformation within the continental lithosphere is strongly dependent on such inherited structures (Butler *et al.*, 2006, and references therein).

Conclusions

The main conclusions of this study are the following:

1. Absolute and relative locations of the 8 June 2008 mainshock and of its aftershocks define a northeast–southwest trending fault with most hypocentral depths in the range 15–25 km. The main event is consistently located at depths 19–24 km if different absolute locations are considered and at 18 km depth after WCC relocation. Similar depths were obtained from the misfit/CLVD-versus-depth curve after the moment tensor inversion, while finite fault inversion results suggest that mainshock waveforms are better fit when using the location derived by the WCC relocation.
2. Moment tensor inversion results indicate that the mainshock had a pure strike-slip mechanism with one nodal plane striking northeast–southwest in accordance with the aftershock locations. Also, this mechanism agrees well with moment tensor solutions that have been published

by different agencies. Some of the largest aftershocks exhibited similar focal mechanisms with some dip-slip component.

3. The preferred slip distribution model for the 8 June earthquake consists of a high slip amplitude patch (~150 cm) beneath the northern part of the fault where most of the damage to buildings was subsequently observed. Smaller patches can be found in the southern part and in deeper parts of the fault. Most of the slip is concentrated at depths between 7 and 20 km, and the relocated aftershocks fill the areas of slip deficit (< 25 cm).
4. Our results, combined with previous seismological and geodetic observations for western Greece, suggest that the 8 June earthquake was caused by the failure of a fault zone that was located at the edge of a clockwise rotating block encompassing Lefkada and Kefalonia Islands, part of mainland Greece, and northwest Peloponnese. It is likely that this zone is inherited from previous tectonic phases and is now reactivated as a strike-slip fault.

Data and Resources

The waveform data that were used in this study were recorded by a nationwide and three regional networks operated by a number of research institutes in Greece. The dataset is not released to the public, and it is only available to these institutes in Greece and their collaborators abroad. The Global Centroid Moment Tensor (CMT) Project database was searched using www.globalcmt.org/CMTsearch.html (last accessed October 2008). Reported moment tensor solutions for the main event were taken from the EMSC–CSEM web page (www.emsc-csem.org) (last accessed October 2008). The moment tensor solutions were calculated using a software package available at http://eqseis.geosc.psu.edu/~cammon/HTML/MTinvDocs/mtinv01.html (last accessed October 2008). Some figures were created using the Generic Mapping Tools (GMT) software package available at www.soest.hawaii.edu/gmt (last accessed October 2008).

Acknowledgments

KIK and SJL would like to thank the National Science Council of Taiwan for the financial support of this study. We are grateful to Denis Hatzfeld, an anonymous reviewer, and associate editor Cezar Trifu for their constructive comments that improved the original manuscript. Thanks are also due to Sofia Rontogianni for discussions about GPS observations and block kinematics in western Greece.

References

Baker, C., D. Hatzfeld, H. Lyon-Caen, E. Papadimitriou, and A. Rigo (1997). Earthquake mechanisms of the Adriatic Sea and western Greece: Implications for the oceanic subduction-continental collision transition, *Geophys. J. Int.* **131,** 559–594.

Benetatos, C., D. Dreger, and A. Kiratzi (2007). Complex and segmented rupture associated with the 14 August 2003 M_w 6.2 Lefkada, Ionian Islands, earthquake, *Bull. Seismol. Soc. Am.* **97,** doi 10.1785/0120060123.

Briole, P., R. Armijo, A. Avalone, P. Bernard, R. Charara, A. Deschamps, D. Dimitrov, P. Elias, R. Grandin, M. Ilieva, S. Lambotte, H. Lyon-Caen, B. Meyer, A. Mouratidis, A. Narcessian, D. Papanastasiou, J. C. Ruegg, E. Sokos, and O. Sykioti (2008). Multidisciplinary study of the June 8, 2008, $M_w = 6.4$ Andravida earthquake, *31st General Assembly,* European Seismol. Commission, Crete, Greece, 327.

Butler, R. W. H., E. Tavarnelli, and M. Grasso (2006). Structural inheritance in mountain belts: Alpine–Apennine perspective, *J. Struct. Geol.* **28,** doi 10.1016/j.jsg.2006.09.006.

Choy, G., and J. L. Boatwright (1995). Global patterns of radiated seismic energy and apparent stress, *J. Geophys. Res.* **100,** 18,205–18,228.

Clément, C., A. Hirn, P. Charvis, M. Sachpazi, and F. Marnelis (2000). Seismic structure and the active Hellenic subduction in the Ionian Islands, *Tectonophysics* **329,** 141–156.

Cocard, M., H.-G. Kahle, Y. Peter, A. Geiger, G. Veis, S. Felekis, D. Paradissis, and H. Biliris (1999). New constraints on the rapid crustal motion of the Aegean region: Recent results inferred from GPS measurements (1993–1998) across the west Hellenic arc, *Earth Planet. Sci. Lett.* **172,** 39–47.

Engdahl, E. R., R. D. van der Hilst, and R. P. Buland (1998). Global teleseismic earthquake relocation with improved travel time and procedures for depth determination, *Bull. Seismol. Soc. Am.* **88,** 722–743.

Evangelidis, C., K. I. Konstantinou, N. S. Melis, M. Charalambakis, and G. N. Stavrakakis (2008). Waveform relocation and focal mechanism analysis of an earthquake swarm in Trichonis Lake, western Greece, *Bull. Seismol. Soc. Am.* **98,** doi 10.1785/0120070185.

Flotté, N., D. Sorel, C. Müller, and J. Tensi (2005). Along strike changes in the structural evolution over a brittle detachment fault: Example of the Pleistocene Corinth–Patras rift (Greece), *Tectonophysics* **403,** doi 10.1016/j.tecto.2005.03.015.

Ghose, S., M. W. Hamburger, and C. J. Ammon (1998). Source parameters of moderate-sized earthquakes in the Tien-Shan, central Asia, from regional moment tensor inversion, *Geophys. Res. Lett.* **25,** 3181–3184.

Goldsworthy, M., J. Jackson, and J. Haines (2002). The continuity of active faults systems in Greece, *Geophys. J. Int.* **148,** 596–618.

Hartzell, S. H., and T. H. Heaton (1983). Inversion of strong ground motion and teleseismic waveform data for the fault rupture history of the 1979 Imperial Valley, California, earthquake, *Bull. Seismol. Soc. Am.* **73,** 1553–1583.

Haslinger, F., E. Kissling, J. Ansorge, D. Hatzfeld, E. Papadimitriou, V. Karakostas, K. Makropoulos, H.-G. Kahle, and Y. Peter (1999). 3D crustal structure from local earthquake tomography around the Gulf of Arta (Ionian region, NW Greece), *Tectonophysics* **304,** 201–218.

Hatzfeld, D., I. Kassaras, D. Panagiotopoulos, D. Amorese, K. Makropoulos, G. Karakaisis, and O. Coutant (1995). Microseismicity and strain pattern in northwestern Greece, *Tectonics* **14,** 773–785.

Hatzfeld, D., G. Pedotti, P. Hatzidimitriou, and K. Makropoulos (1990). The strain pattern in the western Hellenic arc from a microearthquake survey, *Geophys. J. Int.* **101,** 181–202.

Hollenstein, C., M. D. Müller, A. Geiger, and H.-G. Kahle (2008). Crustal motion and deformation in Greece from a decade of GPS measurements, 1993–2003, *Tectonophysics* **449,** doi 10.1016/j.tecto.2007.12.006.

Kagan, Y. Y. (1991). 3-D rotation of double-couple earthquake sources, *Geophys. J. Int.* **106,** 709–716.

Kalogeras, I., D. Loukatos, and G. Stavrakakis (2008). Preliminary report of the strong motion data of the 8 June 2008 earthquake (M_w 6.4) in Achaia–Elia, western Greece, http://www.gein.noa.gr/services/skyros2 (last accessed October 2008).

Kamberis, E., C. Ioakim, S. Tsaila-Monopoli, F. Marnelis, and S. Sotiropoulos (2000). Geodynamic and palaeogeographic evolution of the Ionian area (W. Greece) during upper Cenozoic, *Geol. Soc. Greece Spec. Publ.* **9,** 109–120.

Kamberis, E., S. Sotiropoulos, O. Aximniotou, S. Tsaila-Monopoli, and C. Ioakim (2000). Late Cenozoic deformation of the Gavrovo and Ionian zones in NW Peloponnese (western Greece), *Ann. di Geophys.* **43,** 905–919.

Kennett, B. L. N. (1983). *Seismic Wave Propagation in Stratified Media*, Cambridge U Press, Cambridge.

Klein, F. (2002). User's guide to Hypoinverse2000, a FORTRAN program to solve for earthquake locations and magnitudes, *U.S. Geol. Surv. Open-File Rept. 02-171*.

Konstantinou, K. I., S.-J. Lee, C. P. Evangelidis, and N. S. Melis (2009). Source process and tectonic implications of the 8 January 2006 (M_w 6.7) Kythira earthquake, southern Greece, *Phys. Earth Planet. Interiors* **175,** doi 10.1016/j.pepi.2009.03.010.

Laigle, M., A. Hirn, M. Sachpazi, and C. Clément (2002). Seismic coupling and structure of the Hellenic subduction zone in the Ionian Islands region, *Earth Planet. Sci. Lett.* **200,** 243–253.

Lee, S.-J., K.-F. Ma, and H.-W. Chen (2006). Three-dimensional dense strong motion waveform inversion for the rupture process of the 1999 Chi-Chi, Taiwan, earthquake, *J. Geophys. Res.* **111,** B11308, doi 10.1029/2005JB004097.

Le Pichon, X., N. Chamot-Rooke, S. Lallemant, R. Noomen, and G. Veis (1995). Geodetic determination of the kinematics of central Greece with respect to Europe: Implications for eastern Mediterranean tectonics, *J. Geophys. Res.* **100,** 12,675–12,690.

Lin, G., and P. M. Shearer (2005). Tests of relative earthquake location techniques using synthetic data, *J. Geophys. Res.* **110,** B04304, doi 10.1029/2004JB003380.

Lin, G., and P. M. Shearer (2006). The COMPLOC earthquake location package, *Seism. Res. Lett.* **77,** 440–444.

Margaris, B., C. Papaioannou, N. Theodoulidis, A. Savvaidis, N. Klimis, K. Makra, C. Karakostas, V. Lekidis, T. Makarios, T. Salonikios, M. Demosthenus, G. Athanasopoulos, G. Mylonakis, C. Papantonopoulos, V. Efthymiadou, P. Kloukinas, I. Ordonez, V. Vlachakis, and J. P. Stewart (2008). Preliminary report on the principal seismological and engineering aspects of the $M_w = 6.5$ Achaia-Ilia (Greece) earthquake on 8 June 2008, GEER Association Report No. GEER-013, http://research.eerc.berkeley.edu/projects/GEER/Post_EQ_Reports.html (last accessed October 2008).

Melis, N. S., and K. I. Konstantinou (2006). Real-time seismic monitoring in the Greek region: An example from the 17 October 2005 east Aegean Sea earthquake sequence, *Seism. Res. Lett.* **77,** 364–370.

Melis, N. S., and G.-A. Tselentis (1998). 3-D velocity structure in western Greece determined from tomography using earthquake data recorded at the University of Patras seismic network (PATNET), *Pure Appl. Geophys.* **152,** 329–348.

Melis, N. S., M. Brooks, and R. G. Pearce (1989). A microearthquake study in the Gulf of Patras region, western Greece, and its seismotectonic interpretation, *Geophys. J.* **98,** 515–524.

Melis, N. S., P. W. Burton, and M. Brooks (1995). Coseismic crustal deformation from microseismicity in the Patras area, western Greece, *Geophys. J. Int.* **122,** 815–836.

Newman, A. V., S. Stiros, L. Feng, G. T. Farmer, P. Psimoulis, F. Moschas, and S. Lycourghiotis (2008). Strong rupture and post-seismic response of the 8 June 2008 Andravida earthquake in western Peloponnese, Greece, *31st General Assembly*, European Seismol. Commission, Crete, Greece, 321.

Novotny, O., J. Zahradnik, and G.-A. Tselentis (2001). Northwestern Turkey earthquakes and the crustal structure inferred from surface waves observed in western Greece, *Bull. Seismol. Soc. Am.* **91,** 875–879.

Papazachos, B. C., and K. Papazachou (1997). The earthquakes of Greece, Ziti Editions, Thessaloniki.

Randall, G. E. (1994). Efficient calculation of complete differential seismograms for laterally homogeneous earth models, *Geophys. J. Int.* **118,** 245–254.

Randall, G. E., C. J. Ammon, and T. J. Owens (1995). Moment tensor estimation using regional seismograms from a Tibetan plateau portable network deployment, *Geophys. Res. Lett.* **22,** 1665–1668.

Richards-Dinger, K. B., and P. M. Shearer (2000). Earthquake locations in southern California obtained from source-specific station terms, *J. Geophys. Res.* **105,** 10,939–10,960.

Roumelioti, Z., C. Benetatos, A. Kiratzi, G. Stavrakakis, and N. Melis (2004). A study of the 2 December 2002 (M 5.5) Vartholomio (western Peloponnese, Greece) earthquake and of its largest aftershocks, *Tectonophysics* **387,** 65–79.

Sachpazi, M., A. Hirn, C. Clément, F. Haslinger, M. Laigle, E. Kissling, P. Charvis, Y. Hello, J.-C. Lépine, M. Sapine, and J. Ansorge (2000). Western Hellenic subduction and Cephalonia transform: Local earthquakes and plate transport and strain, *Tectonophysics* **319,** 301–319.

Shearer, P. M. (1997). Improving local earthquake locations using the L1 norm and waveform cross-correlation: Application to the Whittier Narrows, California aftershock sequence, *J. Geophys. Res.* **102,** 8269–8283.

Shearer, P. M., J. L. Hardebeck, L. Astiz, and K. B. Richards-Dinger (2003). Analysis of similar event clusters in aftershocks of the 1994 Northridge, California, earthquake, *J. Geophys. Res.* **108,** no. B1, 2035, doi 10.1029/2001JB000685.

Shearer, P., E. Hauksson, and G. Lin (2005). Southern California hypocenter relocation with waveform cross-correlation, Part 2: Results using source-specific station terms and cluster analysis, *Bull. Seismol. Soc. Am.* **95,** 904–915, doi 10.1785/0120040168.

Sorel, D. (2000). A Pleistocene and still-active detachment fault and the origin of the Corinth–Patras rift, Greece, *Geology* **28,** 83–86.

Stich, D., C. J. Ammon, and J. Morales (2003). Moment tensor solutions for small and moderate earthquakes in the Ibero–Maghreb region, *J. Geophys. Res.* **108,** 2148, doi 10.1029/2002JB002057.

Institute of Geophysics
National Central University
Taoyuan County
Jhongli, 320 Taiwan
kkonst@ncu.edu.tw
(K.I.K.)

Institute of Geodynamics
National Observatory of Athens
Athens, Greece
(N.S.M., C.P.E., K.B.)

Institute of Earth Sciences
Academia Sinica
Taipei, Taiwan
(S.-J.L.)

Manuscript received 14 October 2008